Multi-Scale Imaging of Polymer Electrolyte Fuel Cells using X-ray Micro- and Nano-Computed Tomography, Transmission Electron Microscopy and Helium-Ion Microscopy.

Q. Meyer[1-2], J. Hack[1], N. Mansor[1], F. Iacoviello[1], J. J. Bailey[1], P. R. Shearing[1], D. J. L. Brett*[1]

[1]Electrochemical Innovation Lab, Department of Chemical Engineering, UCL, London, WC1E 7JE, United Kingdom.

[2]Nanoelectrochemistry Group, School of Chemistry, UNSW, Sydney 2000, Australia

[*]Corresponding author: d.brett@ucl.ac.uk

Abstract

Multi-length scale imaging of polymer electrolyte fuel cell (PEFC) membrane electrode assembly (MEA) materials is a powerful tool for studying, understanding and furthering improvements in materials engineering, performance and durability. A hot pressed MEA has been imaged using X-ray micro- and nano-computed tomography (CT), scanning electron microscopy (SEM), transmission electron microscopy (TEM) and recently developed helium-ion microscopy (HeIM). X-ray nano-CT captures a volume containing all of the relevant fuel cell interfaces, from the carbon fibre of the gas diffusion layer (GDL) to the Nafion membrane with a field-of-view of 5 µm and a pixel size of 64 nm. Features identified include linear marks on the carbon fibre surface, agglomerates of carbon nanoparticles in the microporous layer (MPL), and intrusion of the catalyst layer material into the Nafion membrane during the hot-pressing process. HeIM has enabled imaging of a large area of MEA from tens of micrometres to sub-nm pixel, resolution without any sample preparation, and has captured similar features to X-ray micro-CT and nano-CT. Furthermore, at its highest

resolution, the platinum and carbon catalyst nanoparticles can be distinguished at the surface of the catalyst layer, overcoming the limitations of SEM and TEM.

Keywords: Membrane Electrode Assembly (MEA), Gas Diffusion Layer; Catalyst, X-ray Computed Tomography (X-ray CT), Transmission Electron Microscopy (TEM); Helium-ion Microscopy (HeIM)

1 Introduction

Polymer electrolyte fuel cells (PEFCs) fuelled with hydrogen are among the most promising energy conversion technologies for a broad range of applications, including portable, stationary and automotive power delivery. As PEFCs have a complex hierarchical structure, with materials features ranging from nanometres to tens of micrometres, an array of multi-scale imaging techniques is necessary to capture information at the required resolution/scale and to image the interactions and interfaces between materials.

This work highlights the need to adopt different imaging techniques to access different length scales, locations within the membrane electrode assembly (MEA) structure and overcome challenges imposed by sample preparation constraints. In particular, helium-ion microscopy (HeIM) is revealed as a powerful technique for MEA study that has not been applied to PEFCs before.

1.1 The Membrane Electrode Assembly (MEA)

The MEA is composed of an electrolyte membrane sandwiched between the catalyst, gas diffusion layer (GDL) and (usually) a micro-porous layer (MPL) (Figure 1). The electrically conducting, porous gas diffusion layer allows reactant transport to the catalyst and acts as an effective current collector, while also improving hydraulic management by expelling water [1,2]. The structure of the GDL, fibre geometry and porosity [3], as well as the effects of applied compression [4], have been widely investigated to understand how to optimise gas,

water and electron transport. Engineering of GDL materials has been of particular focus, as its structure and polytetrafluoroethylene (PTFE) content directly affect water management and fuel cell performance [5–8]. The GDL is usually composed of carbon fibres around 5-10 μm in diameter, coated with a PTFE/carbon-based micro-porous layer [9]. The electrically conductive nature of the graphitic fibres allows for current collection, while the hydrophobic nature of PTFE provides a means of expelling water from the GDL structure. The catalyst layer (CL), in direct contact with the membrane and the GDL, is typically composed of a thin film (5-20 μm) [10,11] of highly dispersed Pt nanoparticles (~3 nm - 5 nm) deposited on carbon particles (~30 nm - 50 nm) [12,13], with a Nafion ionomer additive to enhance triple-phase boundaries [14,15]. It is either coated onto the microporous medium of the GDL or onto the Nafion membrane, *via* hand-painting, air-brushing, screen-printing or sputtering [16–20]. The fabrication method used imparts different advantages; for example, coating the catalyst layer (CL) directly onto the Nafion membrane can improve the ionic contact at this interface, potentially creating a more extensive electrochemical surface area and lower contact resistance [20].

1.2 Imaging the MEA

Due to the multi-scale aspects of the fuel cell structure, it is impossible to image a statistically relevant number of GDL fibres while also capturing resolved features of the CL and MPL particles in the same field-of-view (FoV) (Figure 2a). As a result, imaging of these materials is typically done separately, using an array of techniques to achieve the target pixel size and sample size compromise, to image the feature of interest (Figure 2b).

Scanning electron microscopy (SEM) and X-ray micro-CT have proven effective in imaging the various layers in the MEA (Figure 2b). SEM has been extensively used to obtain surface structural data, layer thickness, smoothness of different interfaces, the orientation of carbon fibres as well as the PTFE content [2,3,29,30,21–28], CL surface [31], MEA structure

[20,32,33] and aspects of degradation [22]. More recently, X-ray micro-CT has proven to be a useful technique for non-destructive imaging of the MEA by elucidating the internal structure and interfaces in 3-dimensions. X-ray micro-CT has shown to have a sufficiently high resolution (as high as ~190 nm) to image GDLs [4,24,26,34–36]. Furthermore, it has been used to characterise the CL surface features and thickness, deposition methods [16], degradation mechanisms, CL crack length and Pt distribution [14]. Recent work from the authors has linked GDL structure and PTFE content to water distribution using neutron imaging and X-ray micro-CT, along with an analysis of the effect of the hot-pressing temperature on performance and structural changes of CL and Nafion membrane [30,37]. However, neither the SEM nor the X-ray micro-CT is sufficient to image the carbon and Pt nanoparticles or Nafion agglomerates within the CL and MPL.

The analysis of the CL and MPL nanostructures has been performed using a focused ion beam (FIB) lift-out technique [26,14] for sample preparation, and X-ray nano CT for imaging. In this method, a small cube of material (< 25 μm), is cut out of the sample using an ion beam. A small FoV is scanned using X-ray nano-CT, followed by image processing by segmentation with a 16 nm pixel size, and area respectively 2.5 μm -1.5 μm [26,14]. This method has been used to segment the MPL [26], and also study the degradation of the CL, via segmentation of the CL agglomerates from the Nafion ionomer [14] contained in the catalyst ink. However, since the sample is prepared *ex-situ* using this method, relevant information about the structure of the interfaces between the Nafion membrane, catalyst, MPL and GDL cannot be observed as a whole, as the sample is too small to capture it.

At the sub-nanometre scale, individual carbon and Pt nanoparticles, which constitute the MPL and CL, have been successfully characterised using transmission electron microscopy (TEM) [13]. This enables measurement of the catalyst nanoparticles and extraction of statistically relevant information on the particle size and density distribution. However, limitations of

TEM characterisation arise due to the sample preparation; the sample must be sufficiently thin to allow electrons to pass through, which means CL particles must be dispersed onto a transparent sample support. As the sample is not imaged in its original environment, either coated on the MPL or the Nafion membrane, it is not possible to observe a multi-layered CL. The helium ion microscope (HeIM) is a relatively new type of microscopy [38,39]. The HeIM has several advantages over scanning electron microscopy, which includes a high brightness source which is sub-nanometre in size, an enhanced secondary electron yield, restricted beam penetration, and superior image contrast and information content [38,39]. Using this technique, it is theoretically possible to focus the ion beam into a smaller probe size relative to that of the electron beam of an SEM. Hence, resolutions two to four times better than that of comparable SEMs are possible. As such, this equipment provides unique capabilities that push the boundaries of surface microscopy [38,39]. It has the advantage of causing less charging artefacts and damage induced by the beam for small and delicate surface features [40] than SEM. Furthermore, it does not require the sample to be as conductive or require gold coating [41,42]. So far, it has predominately been used to characterise biological samples, nanostructured polymers and for manufacturing nanostructures for nanoelectronics/energy storage [40,43–45]. However, the advantages of this technique make it potentially attractive to image a complex multi-layered structure with electrically conducting materials (carbon, Pt), and insulating materials (Nafion, PTFE), such as those found in PEFCs. It has been recently used to characterise the electrode materials with different polymer content, before and after accelerated degradations [46].

In light of some of the current limitations of MEA imaging, either by destructive sample preparation or by insufficient internal imaging capabilities, the current work aims to provide a full characterisation of the MEA interfacial area from the micro- to the sub-nanoscale, correlating data from CT, HeIM and TEM. This work bridges the gap between the micro- and

nano-scale, by imaging an MEA using a combination of X-ray nano-CT and micro-CT, He-ion microscopy and TEM and provides new sight into the structure of the MEA, examining the capabilities of each technique for capturing information about the MEA across a range of length scales.

2 Experimental

2.1 Material

Full- and half-MEAs were prepared in-house for X-ray micro-CT, HeIM, SEM, and X-ray nano-CT studies, respectively. Nafion NRE-212 membrane (Dupont, USA) was used without pre-treatment. Johnson Matthey ELE0162 GDEs (gas diffusion layer coated with MPL and 0.4 mg_{Pt} cm^{-2} CL) were used, and the membrane was hot-pressed onto either a single electrode or two electrodes, with an active area of 5.29 cm^2. The GDE is hot-pressed on the Nafion membrane for 3 min with an applied pressure of 2757 kPa at 130 °C. These conditions are identical to previously published work which showed these conditions resulted in optimal performance [37]. Building a half-cell for nanoscale work (Figure 1b) instead of a full cell provides stronger structural integrity, limiting the risk of delamination of the GDL when machined into smaller samples. Fresh MEA samples of identical type were prepared for each characterisation technique used.

2.2 Characterisation Techniques.

2.2.1 X-ray micro-CT

The MEA was prepared via probing a 1 mm disk using a biopsy punch out of a 5.29 cm^2 MEA. A disk shape is preferable to optimise the image collection process and maximise the signal-to-noise ratio, by ensuring that the maximum amount of sample was in the FoV and that there was uniform penetration of X-rays through every projected angle of the scan. The sample was then mounted on a pin-head using carbon tape. A laboratory X-ray micro-CT system, ZEISS Xradia 520 Versa (Carl Zeiss, USA) was used for 3D imaging. A source

voltage of 90 kV and a FoV of 700 μm × 700 μm were used for the sample. 3701 projections were captured with an exposure time of 12 s. Reconstruction of the radiographs into a 3D volume was achieved using a cone-beam filtered back-projection algorithm (Reconstructor Scout-and-Scan, ZEISS) resulting in a series of ortho-slices containing slice data in all three planes (xy, xz, yz) with isotropic voxel size of ~372 nm.

2.2.2 X-ray nano-CT

A half-MEA was initially prepared via probing a 0.5 mm disk using a biopsy punch out of a 5.29 cm^2 MEA, and then cut into smaller samples under an optical microscope using a scalpel, until the sample dimensions reached 50 μm × 50 μm × 80 μm. It was then mounted on a needle head using epoxy. A laboratory X-ray nano-CT system, ZEISS Xradia 810 Ultra (Carl Zeiss, USA) was used for 3D imaging. The large field-of-view (LFoV) mode was used (65 μm × 65 μm). 2001 projections were captured with an exposure time of 30 s. Reconstruction of the radiographs into a 3D volume was achieved using a quasi-parallel filtered back-projection algorithm (Reconstructor Scout-and-Scan, ZEISS), resulting in an isotropic voxel size of ~63 nm). Imaging of the Nafion with X-ray nano-CT causes damage to the Nafion membrane, with a sample drift of 3 nm min-1 measured here. The sample shift is limited and can be corrected using the adaptive motion correction [47].

2.2.3 X-ray post-processing

For all reconstructed volumes, post-processing and image segmentation were performed using Avizo Lite (Thermo Fisher, Bordeaux, France) to segment the GDL layer material, consisting of large fibres bonded with PTFE, from the micro-porous medium, CL medium and the Nafion polymer membrane. A FoV of 32 μm × 32 μm in the *x-y* orientation was chosen for material segmentation and analysis for the X-ray nano-CT sample, and 400 μm × 400 μm in the *x-y* orientation for the X-ray micro-CT sample. Similar strategies were used for the

micro- and nano-CT segmentation: the CL ink, composed of carbon / PTFE / Pt / Nafion, much denser, is segmented via grayscale thresholding. The Nafion membrane, underneath the CL is isolated using 'Magic Wand' segmentation (Avizo segmentation toolkit), visible due to the change of contrast. Finally, the MPL can be seen as the lighter material surrounding the CL and the fibres. On the larger X-ray micro-CT sample, the MPL has not been segmented from the fibres, due to the challenges of the accurate segmentation. However, it has been achieved on the smaller volume as an illustration of the pixel limitations and signal-to-noise ratio, causing uncertainty.

2.2.4 Helium Ion Microscope (HeIM).

For HeIM imaging, the GDE/MEA was cut into circular samples of 5 mm diameter and attached to adhesive carbon disks. These samples were investigated using a Zeiss Orion Plus™ HeIM. The helium ion accelerating voltage was approximately 30 kV, with an Everhart–Thornley (ET) detector collecting secondary electrons with a positive grid bias of 500 V, with FoV ranging from 12 µm to 700 nm.

2.2.5 Scanning electron microscopy (SEM).

For SEM imaging, the GDE was cut into circular samples of 5 mm diameter and attached to adhesive carbon disks. This sample was investigated using an EVO MA 10 (Carl Zeiss, USA) SEM with EDS (Inca X-act, Oxford Instruments). SEM micrographs were taken of the longitudinal section. At high magnification, an electron accelerating voltage of 10-20 kV and the use of a lateral secondary electron detector enabled the imaging of carbon nanoparticles of the CL with a pixel resolution of ~51 nm.

2.2.6 Transmission Electron Microscopy (TEM)

For TEM imaging, the particles were scratched from the GDE surface using a spatula, diluted in methanol, and then deposited onto a holey carbon copper grid. TEM images were taken

using a JEOL JEM2010 instrument operating at 200 kV, equipped with a Gatan Orius camera system.

3 Results and Discussion

Using X-ray micro-CT, the large FoV provides information regarding the spatial distribution of the carbon fibres of the GDL and information about macro-features of the CL and Nafion deformations can be obtained (Figure 3a). The area scanned is larger than the representative equivalent area of 0.1 mm2 [37]; hence, the observations are representative and do not describe isolated features. Thus, it is possible to calculate the porosity across the fibres in multiple directions, the interfacial contact between the layers (CL/GDL, MPL/CL, Nafion/CL and Nafion/GDL), the CL crack size and the Nafion roughness factor [37].

However, this resolution is not sufficient to enable observation of features on the carbon fibres / MPL, which both appear highly pixelated (Figure 3b). In addition, it is difficult to observe from this image the quality of the contact between the CL and the Nafion membrane. The imaging limitations are in agreement with the orthoslices (Figure 4a and c), showing the lack of resolved features at the interface. Furthermore, the features of the MPL/CL, combined with the pixel size, correspond to the blue area of Figure 2, with a pixel size in the same range as the size of the features of interest. Although the SEM (Figure 3c) provides a better insight into the structure, with MPL nanoparticle agglomerate distinguishable, it is difficult to focus on these particles while imaging the fibre at the same time.

Therefore, an alternate approach has been used to image the same area, yet at a significantly higher resolution with X-ray nano-CT and the HeIM. The improvement in image resolution from X-ray micro-CT to X-ray nano-CT can be seen in the reconstructed orthoslices (Figure 4), with nearly six-times higher voxel resolution taken from similar locations on the samples imaged for micro-CT and nano-CT. Specifically, the fibre shape and its edges are far more visible, along with the Nafion / CL / MPL interfaces visible as a line (Figure 4c-d) instead of

a blurry interfacial area (Figure 4b) challenging to reliably segment, and features of the MPL distinguishable from the background instead of observing it as a block. Indeed, X-ray nano-CT reveals MPL agglomerates of particles (200-500 nm) and a change of porosity between the MPL and CL (Figure 5a). These observations are supported by the HeIM images (Figure 5b-d), showing how the fibre is covered by the MPL and CL, and revealing the porosity gradient between the MPL and CL (Figure 5b). The difference in density and porosity of particles can also be confirmed in the TEM image (Figure 5e). The smaller and more densely packed carbon particles with high quantity of Pt nanoparticles (darker particles about ~5 nm in size) corresponding to the CL, whereas the larger and less dense carbon particles are from the MPL. This implies that the CL has been coated onto the MPL as an ink, entering the pores and forming a denser layer on top of the MPL, creating a gradient between the two materials in porosity and Pt content. Imaging the Nafion / CL interface with X-ray nano-CT also reveals the presence of interfacial features (0.5-2 μm) bonding the phases together. As the catalyst surface is rougher than the Nafion surface (with respective roughness factors of 1.54 and 1.02 [37] reported using micro-CT and AFM), subsequent deformations and intrusions of both materials into one-another occur during the hot-pressing process. Once the heat and pressure are removed, the two materials remain partially attached to each other (Figure 5a), with areas fully bonded together; whereas other localised areas highlight no contact between the two surfaces, due to the depth of the cracks in the CL. Although the agglomerates of carbon from the MPL are visible, single particles cannot be observed with X-ray nano-CT. Another feature is the linear marks on the carbon fibre, observable with X-ray CT (Figure 5a) and HeIM (Figure 5b, Figure 5d). The presence of these features, and their width/depths into the fibres, could potentially affect the way the MPL / GDL interface behaves over time. Specifically, increasing the depth of the striation marks during manufacturing could increase the quality of the contact between the MPL and the carbon fibres, and lower the internal

resistance between these layers after coating. To the authors' knowledge, this is the first time the fibre / CL / MPL / Nafion interfaces has been imaged with X-ray nano-CT with this resolution, and the first time the HeIM has been used to correlate the observations of two different techniques (marks on the fibres with X-CT, density of the particles with TEM) and offer further sight into the membrane electrode assembly structure. Imaging of the carbon particles (CL/MPL) has been achieved using the HeIM. The carbon nanoparticles, across the same sample, appear either densely packed, yet easily distinguishable (Figure 6b), or engulfed in a matrix-like structure, (Figure 6c). This structure could be solidified Nafion, as reported by Chiarev et al. [46]. However, the vast discrepancy between Figure 6b-csuggests that although an ionomer ink with a known Nafion content is added to the catalyst ink, local Nafion heterogenous concentrations exist within the solidified catalyst layer [48]. Specifically, Nafion is concentrated in areas less dense in nanoparticles, which could form additional pathways for the proton and water transport across the catalyst layer, creating a effective 3-D electrode. To assess the ability of HeIM to image Pt nanoparticles coated on carbon nanoparticles, the HeIM was used at its highest resolution and correlated with TEM. The HeIM reveals small bright particles coated onto the carbon nanoparticles of expected size range for Pt nanoparticles [49]. In the process of imaging catalyst nanoparticles in technological MEAs, they are typically imaged before coating onto the MPL [12]. The HeIM pixel resolution (~0.6 nm) can only provide a crude image of the Pt nanoparticles and is not sufficient to measure the particle size with the accuracy of TEM (Figure 2, Figure 6b-d). However, there are challenges with TEM imaging. The Pt density varies significantly between TEM images (low in Figure 7b, intermediate in Figure 7c and saturated in Figure 7d). This Pt apparent heterogeneous distribution does not reflect the actual Pt density distribution across the sample, but instead is an artefact created by the sample preparation, in which the CL/MPL is disrupted when a physical blade cutting sectioning is used. This can lead to distortion of the

sample structure and ‘streaking’ of the chemical composition across the face of the cut. This highlights the challenges of having a sample thin enough to image a single layer of carbon particles with TEM, after coating onto a thick, yet porous MPL, and distinguish the CL/MPL interface. On the other hand, the HeIM enables the imaging of the catalyst after coating onto the MPL. It is possible to distinguish the two materials, and the resolution enables to carbon particles with Pt catalyst to be distinguished from carbon particles of the MPL. Furthermore, the HeIM could enable to observe the CL particle density distribution after coating onto this MPL. This imaging method can be used to assess the effect of the catalyst ink preparation and deposition method onto the MPL to quality of the CL/MPL interface.

4 Conclusions

Multi-scale characterisation of MEAs provides the opportunity for gaining an in-depth insight into the interfaces and structural features of the MEA layer structure. This paper demonstrates the necessity of imaging samples taken from a fully assembled MEA, instead of probing and imaging subsystems, such as the CL coated onto the MPL, or MPL interactions with the GDL. This imaging study reveals new features, such as how the Nafion and CL are bonded together, how the CL is coated onto the MPL, how the carbon fibres influence the structure, and the patterning of the carbon fibres.

Different techniques reveal varying information, depending on the properties of interest. For the first time, the combination of X-ray nano-CT, HeIM and TEM microscopy has been applied to the study of PEFC MEAs, and enables to draw a relevant comparison across these techniques, and highlight their advantages and disadvantages. Over the other imaging techniques, the HeIM is superior as it has the combination of the following capabilities:

- Imaging of insulating sample enabling it to image PTFE and Nafion with high resolution.

- Imaging without coating at highest resolution with better contrast and improved depth of focus than SEM.
- High surface sensitivity.
- Imaging of ultra-thin layers, enabling imaging of the catalyst layer.
- Resist patterning.
- No image processing compared with computed tomography.

Furthermore, the HeIM microscope has been able to capable features identifiable using the other techniques, overcoming the resolution, signal-to-noise ratio of the X-ray micro-CT and nano-CT, the challenges of the depth-of-field of the SEM, and the inherent limitations of TEM as a transmission technique. These are directly relevant to understand the interactions between the different materials. The systematic cross-instrument methodologies used for imaging in this study are also directly relevant for other electrochemical materials, such as Li-ion batteries electrodes and solid electrolytes.

Acknowledgments

The authors would like to acknowledge the EPSRC for supporting the Electrochemical Innovation Lab through (EP/M009394/1, EP/G030995/1, EP/I037024/1, EP/M014371/1 and EP/M023508/1). PRS acknowledges funding from the Royal Academy of Engineering. We thank Dr. Suguo Huo and the London Centre for Nanotechnology at University College London for the collection of the HeIM data.

References

[1] M. W. Reed, R. J. Brodd, *Carbon.* **1965**, *3*, 241.

[2] U. Pasaogullari, C. Y. Wang, *J. Electrochem. Soc.* **2004**, *151*, A399.

[3] O. S. Burheim, J. G. Pharoah, H. Lampert, P. J. S. Vie, S. Kjelstrup, *J. Fuel Cell Sci. Technol.* **2011**, *8*, 021013.

[4] J. P. James, H.-W. Choi, J. G. Pharoah, *Int. J. Hydrogen Energy* **2012**, *37*, 18216.

[5] J.-C. Tsai, C.-K. Lin, *J. Taiwan Inst. Chem. Eng.* **2011**, *42*, 945.

[6] M. V. Williams, E. Begg, L. Bonville, H. R. Kunz, J. M. Fenton, *J. Electrochem. Soc.* **2004**, *151*, A1173.

[7] H. Li, Y. Tang, Z. Wang, Z. Shi, S. Wu, D. Song, J. J. Zhang, K. Fatih, J. J. Zhang, H. Wang, Z. Liu, R. Abouatallah, A. Mazza, *J. Power Sources* **2008**, *178*, 103.

[8] S. Park, J.-W. W. Lee, B. N. Popov, *Int. J. Hydrogen Energy* **2012**, *37*, 5850.

[9] A. Z. Weber, J. Newman, *J. Electrochem. Soc.* **2005**, *152*, A677.

[10] M. S. Wilson, J. A. Valerio, S. Gottesfeld, *Electrochim. Acta* **1995**, *40*, 355.

[11] A. Suzuki, T. Hattori, R. Miura, H. Tsuboi, N. Hatakeyama, H. Takaba, M. C. Williams, A. Miyamoto, *Int. J. Electrochem. Sci.* **2010**, *5*, 1948.

[12] N. Mansor, A. Belen Jorge, F. Corà, C. Gibbs, R. Jervis, P. F. McMillan, X. Wang, D. J. L. Brett, *ECS Trans.* **2013**, *58*, 1767.

[13] N. Mansor, A. B. Jorge, F. Corà, C. Gibbs, R. Jervis, P. F. McMillan, X. Wang, D. J. L. Brett, *J. Phys. Chem. C* **2014**, *118*, 6831.

[14] A. Pokhrel, M. El Hannach, F. P. Orfino, M. Dutta, E. Kjeang, *J. Power Sources* **2016**, *329*, 330.

[15] M. Wilson, S. Gottesfeld, *J. Appl. Electrochem.* **1992**, *22*, 1.

[16] H. R. Q. Jhong, F. R. Brushett, P. J. A. A. Kenis, *Adv. Energy Mater.* **2013**, *3*, 589.

[17] A. T. Haug, R. E. White, J. W. Weidner, W. Huang, S. Shi, T. Stoner, N. Rana, *J. Electrochem. Soc.* **2002**, *149*, A280.

[18] A. Strong, C. Thornberry, S. Beattie, R. Chen, S. R. Coles, *J. Fuel Cell Sci. Technol.* **2015**, *12*, 1.

[19] H. Tang, S. Wang, S. P. Jiang, M. Pan, *J. Power Sources* **2007**, *170*, 140.

[20] M. Prasanna, E. A. Cho, T. H. Lim, I. H. Oh, *Electrochim. Acta* **2008**, *53*, 5434.

[21] D. Gerteisen, T. Heilmann, C. Ziegler, *J. Power Sources* **2009**, *187*, 165.

[22] R. A. Silva, T. Hashimoto, G. E. Thompson, C. M. Rangel, *Int. J. Hydrogen Energy* **2012**, *37*, 7299.

[23] T. J. Mason, J. Millichamp, T. P. Neville, A. El-kharouf, B. G. Pollet, D. J. L. Brett, *J. Power Sources* **2012**, *219*, 52.

[24] S. Odaya, R. K. Phillips, Y. Sharma, J. Bellerive, A. B. Phillion, M. Hoorfar, *Electrochim. Acta* **2015**, *152*, 464.

[25] J. Yu, Z. Jiang, M. Hou, D. Liang, Y. Xiao, M. Dou, Z. Shao, B. Yi, *J. Power Sources* **2014**, *246*, 90.

[26] H. Ostadi, P. Rama, Y. Liu, R. Chen, X. X. Zhang, K. Jiang, *J. Memb. Sci.* **2010**, *351*, 69.

[27] H. Ito, T. Iwamura, S. Someya, T. Munakata, A. Nakano, Y. Heo, M. Ishida, H. Nakajima, T. Kitahara, *J. Power Sources* **2016**, *306*, 289.

[28] A. Pfrang, D. Veyret, F. Sieker, G. Tsotridis, *Int. J. Hydrogen Energy* **2010**, *35*, 3751.

[29] F. E. Hizir, S. O. Ural, E. C. Kumbur, M. M. Mench, *J. Power Sources* **2010**, *195*, 3463.

[30] Q. Meyer, S. Ashton, P. Boillat, M. Cochet, E. Engebretsen, D. P. Finegan, X. Lu, J. Bailey, N. Mansor, R. Abdulaziz, O. Taiwo, R. Jervis, S. Torija, P. Benson, S. Foster, P. Adcock, P. R. Shearing, D. J. L. Brett, *Electrochim. Acta* **2016**, *211*, 478.

[31] J. Yu, M. N. Islam, T. Matsuura, M. Tamano, Y. Hayashi, M. Hori, *Electrochem. Solid-State Lett.* **2005**, *8*, A320.

[32] A. Therdthianwong, P. Manomayidthikarn, S. Therdthianwong, *Energy* **2007**, *32*, 2401.

[33] S. Martemianov, V. A. Raileanu Ilie, C. Coutanceau, *J. Solid State Electrochem.* **2014**, *18*, 1261.

[34] H. Ostadi, P. Rama, Y. Liu, R. Chen, X. X. Zhang, K. Jiang, *Chem. Eng. Sci.* **2010**, *65*, 2213.

[35] T. Koido, T. Furusawa, K. Moriyama, *J. Power Sources* **2008**, *175*, 127.

[36] A. Pfrang, S. Didas, G. Tsotridis, *J. Power Sources* **2013**, *235*, 81.

[37] Q. Meyer, N. Mansor, F. Iacoviello, P. L. Cullen, R. Jervis, D. Finegan, C. Tan, J. Bailey, P. R. Shearing, D. J. L. Brett, *Electrochim. Acta* **2017**, *242*, 125.

[38] R. Hill, F. H. M. Faridur Rahman, *Nucl. Instruments Methods Phys. Res. Sect. A Accel. Spectrometers, Detect. Assoc. Equip.* **2011**, *645*, 96.

[39] K. Ohya, T. Yamanaka, K. Inai, T. Ishitani, *Nucl. Instruments Methods Phys. Res. Sect. B Beam Interact. with Mater. Atoms* **2009**, *267*, 584.

[40] M. S. Joens, C. Huynh, J. M. Kasuboski, D. Ferranti, Y. J. Sigal, F. Zeitvogel, M. Obst, C. J. Burkhardt, K. P. Curran, S. H. Chalasani, L. a Stern, B. Goetze, J. A. J. Fitzpatrick, *Sci. Rep.* **2013**, *3*, 1.

[41] A. Beyer, H. Vieker, R. Klett, H. M. zu Theenhausen, P. Angelova, A. ölzhäuser, *Beilstein J. Nanotechnol.* **2015**, *6*, 1712.

[42] G. Hlawacek, V. Veligura, R. van Gastel, B. Poelsema, *J. Vac. Sci. Technol. B* **2014**, *32*, 20801.

[43] V. N. Bliznyuk, D. LaJeunesse, A. Boseman, *Nanotechnol. Rev.* **2014**, *3*, 361.

[44] M. T. Postek, A. E. Vladár, *Scanning* **2008**, *30*, 457.

[45] B. Goetze, C. Huynh, L. Stern, H. Wu, D. Ferranti, M. Ananth, *Microsc. Microanal.* **2013**, *19*, 908.

[46] S. Chiriaev, N. Dam Madsen, H.-G. Rubahn, S. Ma Andersen, *AIMS Mater. Sci.* **2017**, *4*, 1289.

[47] A. Sasov, X. Liu, P. L. Salmon, In *Developments in X-Ray Tomography VI*; 2008; Vol. 7078, p. 70781C.

[48] A. Li, M. Han, S. H. Chan, N. Nguyen, *Electrochim. Acta* **2010**, *55*, 2706.

[49] S. Thiele, T. Fürstenhaupt, D. Banham, T. Hutzenlaub, V. Birss, C. Ziegler, R. Zengerle, *J. Power Sources* **2013**, *228*, 185.

Figure Captions

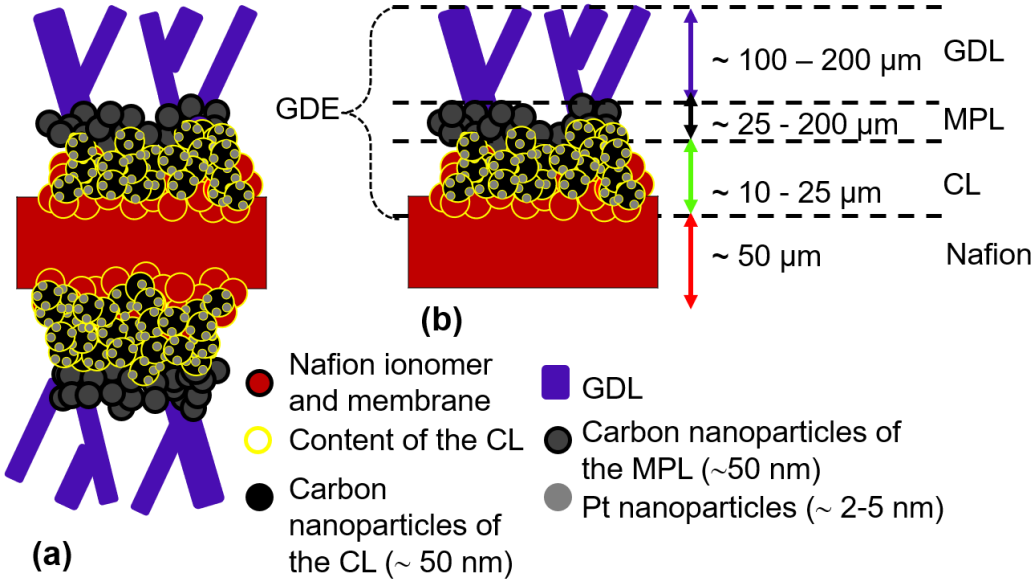

Figure 1: (a) Schematic of the MEA showing the distributed interface between different components and (b) their typical thicknesses for each component / layer.

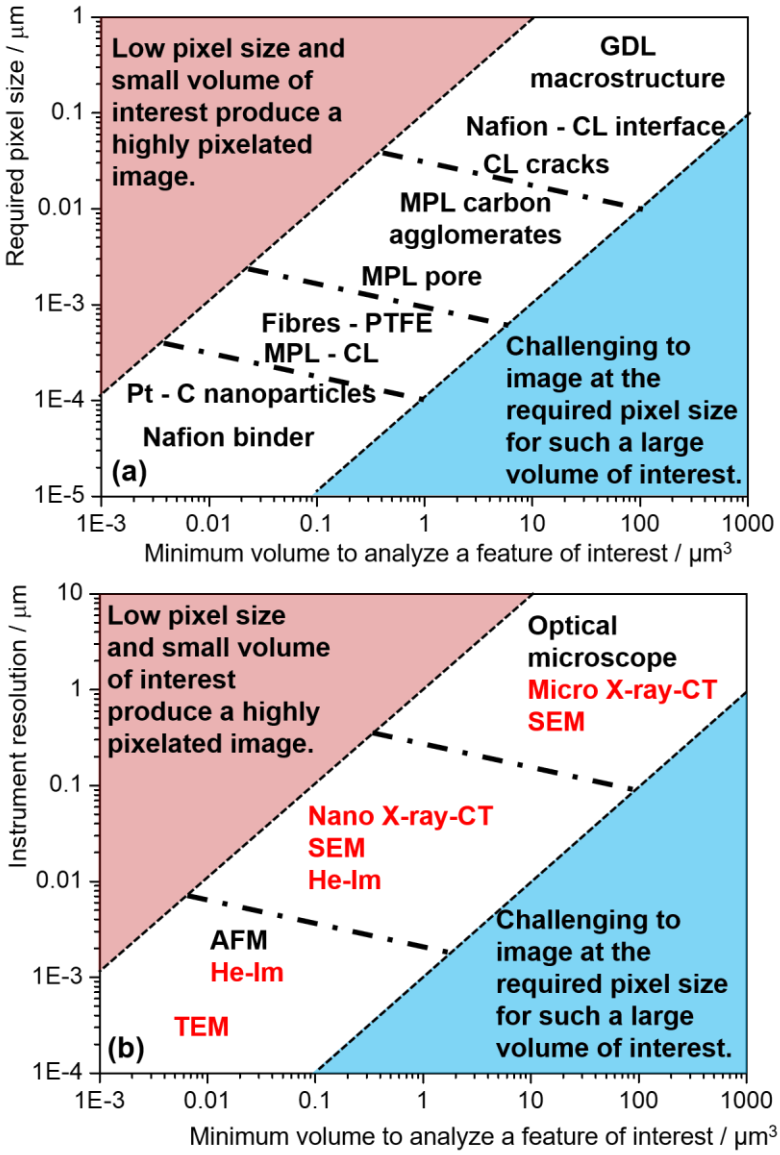

Figure 2: (a) Correlation between the minimum volume to analyse a feature of interest for statistical relevance, pixel size and features of interest of the MEA; (b) relevant instruments (non-exhaustive list) capable of reaching these targets.

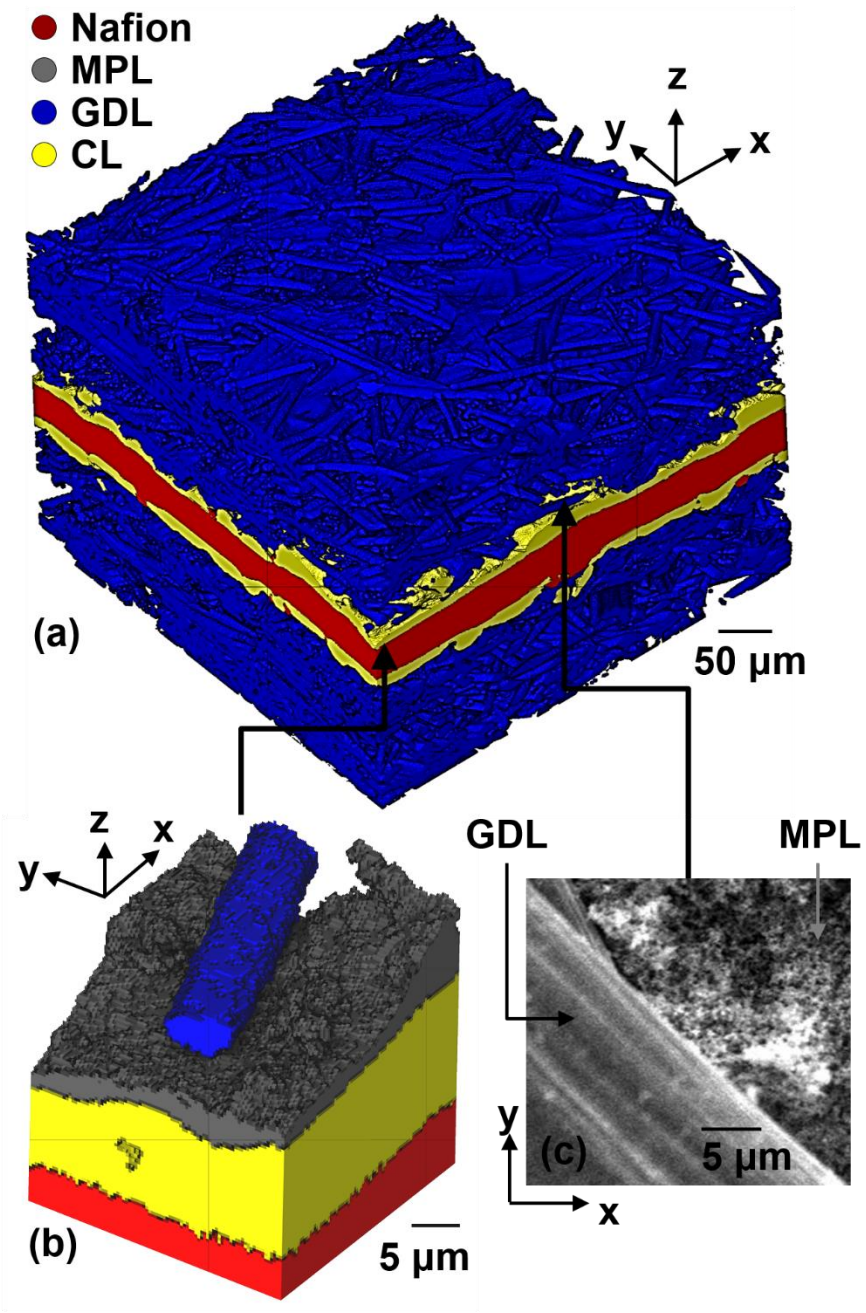

Figure 3: Imaging of a hot-pressed fuel cell with pixel size from 372 nm to 51 nm. (a) Segmented CL, GDL and Nafion using X-ray µ-CT (FoV: 400 µm × 400 µm × 1000 µm, pixel size: 372 nm); (b) segmented GDL, CL, MPL and Nafion using X-ray micro-CT (FoV: 32 µm × 32 µm × 42 µm, pixel size: 372 nm); (c) SEM image of the MPL and carbon fibres (FoV: 30 µm × 27 µm, pixel size: 51 nm).

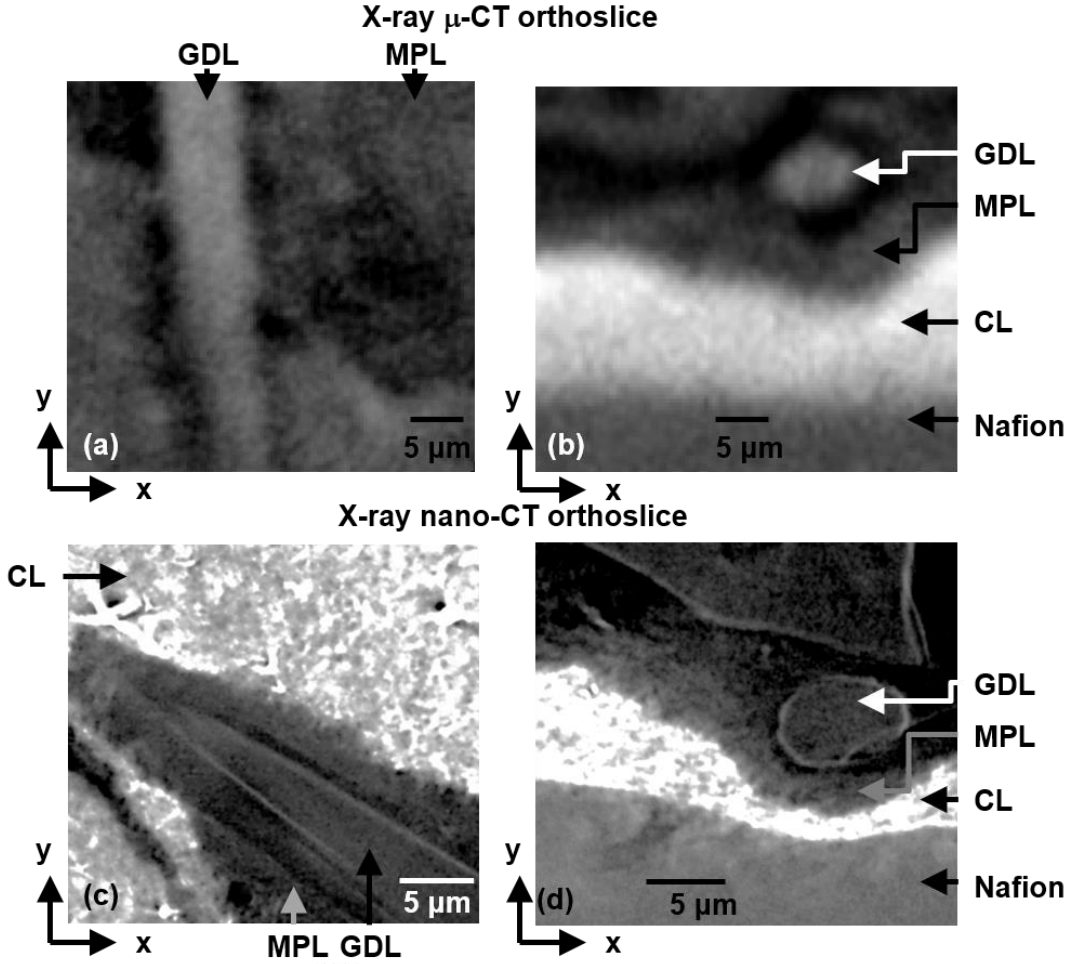

Figure 4: (a-b) X-ray orthoslice of two similar samples of the hot-pressed fuel cell. Micro-CT (pixel size: 372 nm); (c-d) nano-CT (pixel size: 63 nm).

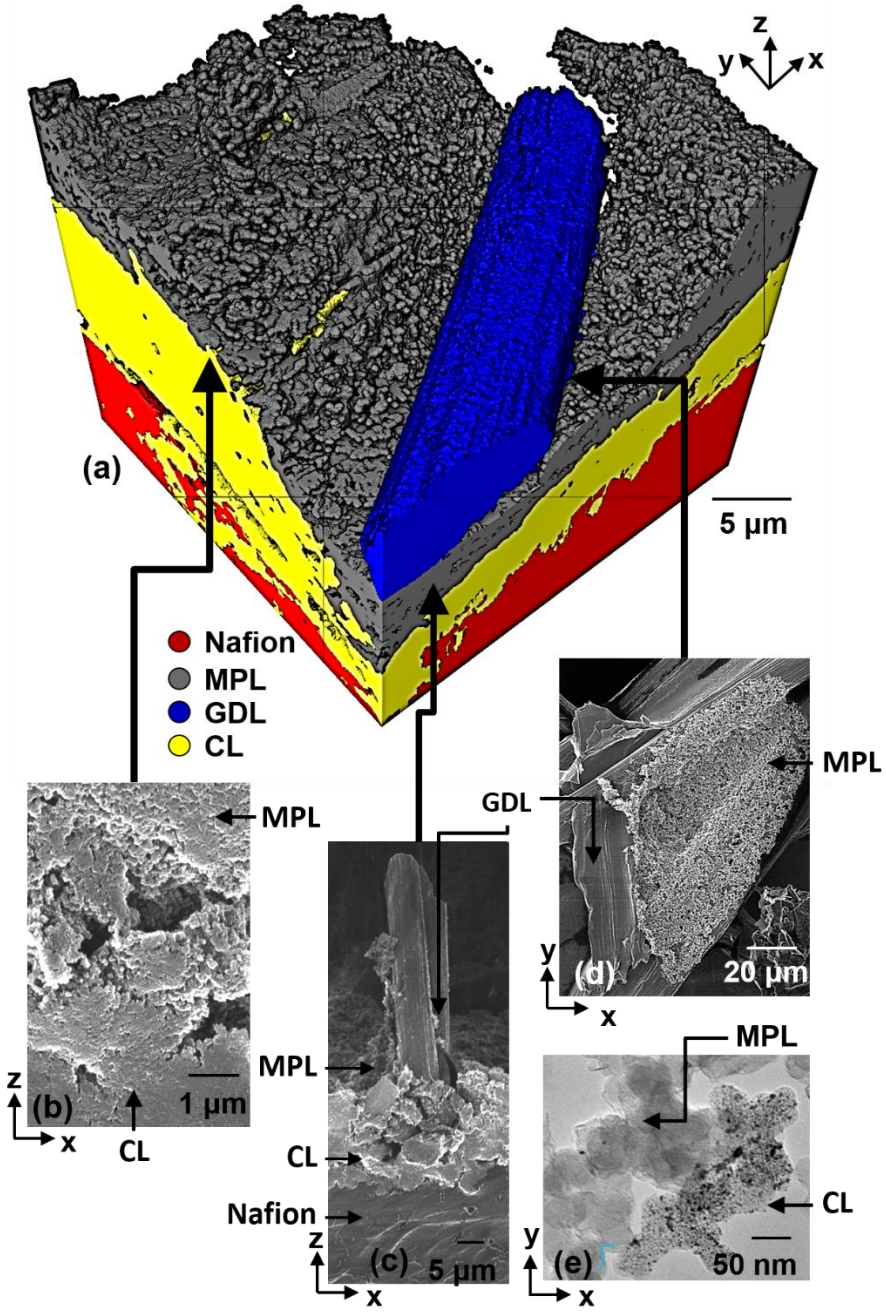

Figure 5: Imaging of fuel cell materials with pixel size from 63 nm to 0.17 nm. (a) Segmented volume rendering of the MEA (FoV: 32 µm × 32 µm, pixel size: 63 nm); (b) HeIM image of the interface GDL/MPL (FoV: 100 µm × 130 µm, pixel size: 61 nm); (c) MPL/CL (FoV: 7 µm × 5 µm, pixel size: 7 nm); (d) fibre / MPL / CL / Nafion (FoV: 32 µm × 77 µm, pixel size: 63 nm); (e) TEM image of the CL and MPL particles (FoV: 340 nm × 285 nm, pixel size: 0.17 nm).

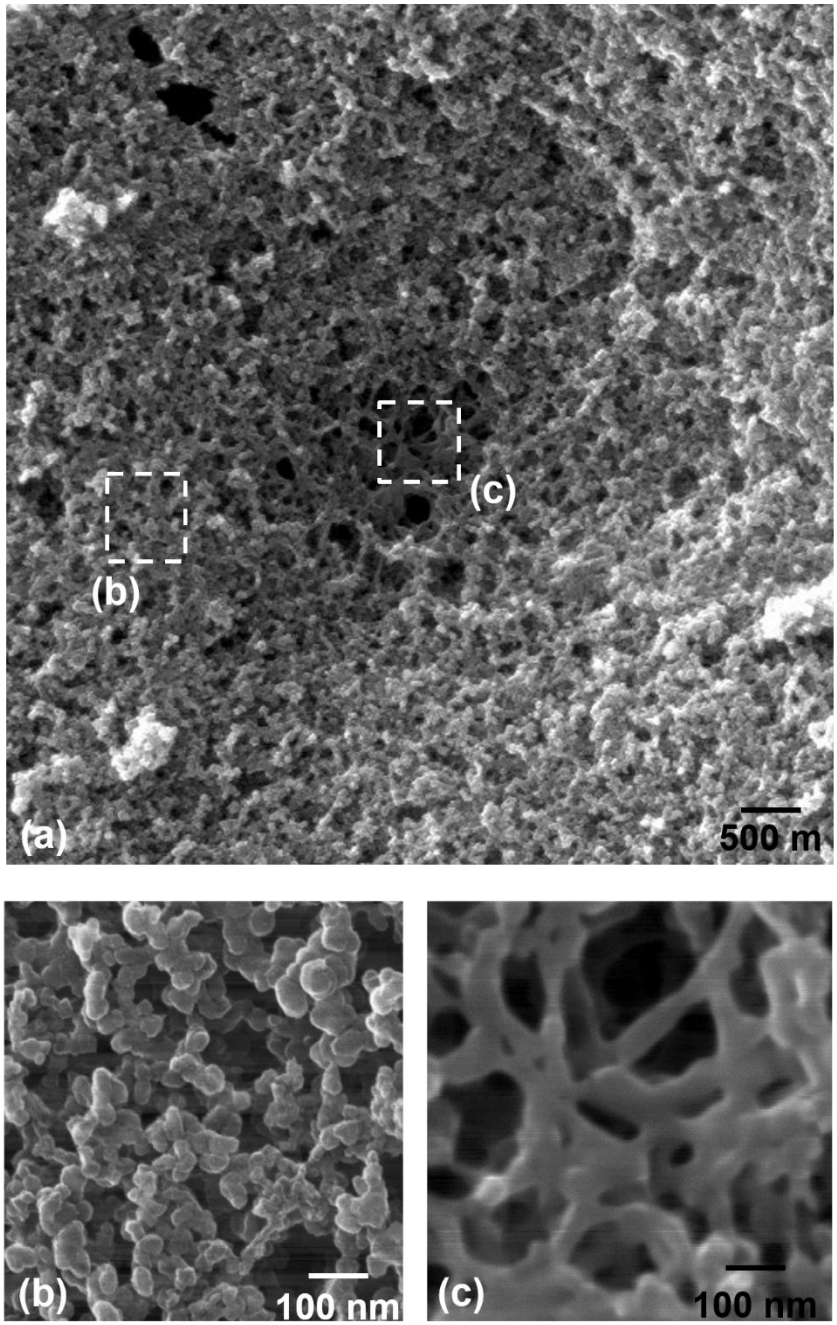

Figure 6: Imaging of the CL coated on the MPL with pixel size from 10 nm to 1.2 nm with HeIM; (a) wide-scale structure of the CL (FoV: 7 μm × 7 μm, pixel size: 10 nm); (b-c) focus on nanofeatures (FoV: 660 nm × 660 nm, pixel size: 1.5 nm).

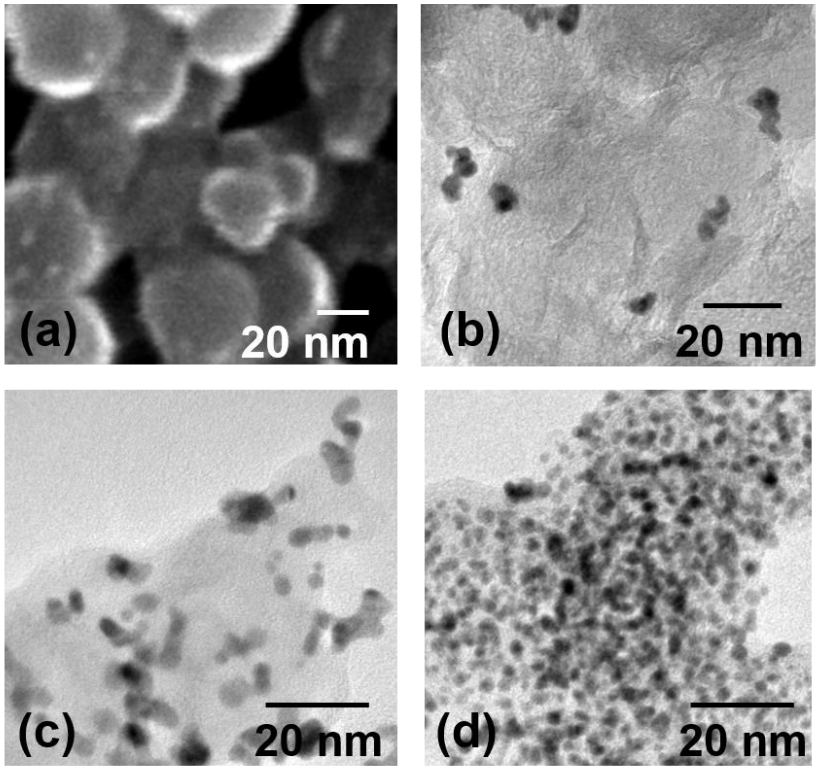

Figure 7: Imaging of the Pt nanoparticles coated on carbon nanoparticles with pixel size from 0.5 nm to 0.05 nm. (a) Imaging with the HeIM (FoV: 150 nm × 150 nm, pixel size: 0.5 nm); (b-d) imaging with TEM (b: FoV: 100 nm × 100 nm, pixel size: 0.08 nm, c-d, FoV: 75 nm × 75 nm, pixel size: 0.05 nm).